Interfacial debonding and cracking in a solid propellant composite under uniaxial tension: An *in situ* synchrotron X-ray tomography study

G.D. Lai [a], L.P. Sang [d], Y.L. Bian [c], H.L. Xie [e], J.H. Liu [f], H.W. Chai [b,*]

[a] *School of Physical Science and Technology, Southwest Jiaotong University, Chengdu, Sichuan, PR China*
[b] *Dynamic Materials Data Science Center, Southwest Jiaotong University, Chengdu, Sichuan, PR China*
[c] *The Peac Institute of Multiscale Sciences, Chengdu, Sichuan, PR China*
[d] *Science and Technology on Aerospace Chemical Power Laboratory, Hubei Institute of Aerospace Chemotechnology, Xiangyang, Hubei, PR China*
[e] *Shanghai Synchrotron Radiation Facility, Shanghai Advanced Research Institute, Chinese Academy of Sciences, Shanghai, PR China*
[f] *Chengdu JiangDe Technology Co., Ltd, Chengdu, Sichuan 610100, PR China*

ARTICLE INFO

ABSTRACT

Deformation and fracture of a hydroxyl-terminated polybutadiene (HTPB)/ammonium perchlorate (AP)/aluminum solid propellant under quasi-static tensile loading are investigated by *in situ* synchrotron X-ray micro computed tomography (CT) and CT-image-based finite element method (FEM) modeling. Bulk stress–strain curve of the solid propellant, and the evolution of particle morphology, and mesoscale strain and particle displacement fields are obtained. Based on tracking and statistics, an automated analytical method is proposed to analyze the relationship between microcrack nucleation and initial structure. The AP particles undergo negligible deformation and orientation changes during tensile loading. Microcracks are mainly nucleated via tension-induced debonding at the maximum surface curvature of the AP particles, and propagate along the curvature gradient around AP particles. Larger AP particles are more prone to debond, and Al particles play a negligible role in deformation and fracture.

Contents

---

1. Introduction

Solid propellants are composed of energetic crystals, polymer binders, metal particles oxidants and stabilizers [1]. Given their simple production, convenient storage, stable structure and other useful characteristics, solid propellants are widely used in aerospace, defense industry and other fields [2–5]. In particular, hydroxy-terminated polybutadiene (HTPB) as a widely used binder for composite solid propellants due to its low viscosity, high aging resistance, wide range of burn rate adjustability, and excellent mechanical properties and stability. In addition, HTPB can be further stabilized under extreme acceleration conditions by enhancing the crosslinking density, optimizing the binder, and improving the self-healing ability of the interface [6–9]. However, solid propellants with heterogeneous phases frequently undergo different extreme conditions during manufacture, storage, transportation and service, giving rise to degradation in microstructure and properties, and the difficulty in accurately predicting their performance. Therefore, maintaining structural integrity of solid propellants and knowledge on their structure–property relations are critical to their applications and safety issues.

Stress–strain curve analysis is one of the widely used methods [10–12] for characterizing composite materials including solid propellants, and can be combined with various *in situ* diagnostics. Van Ramshorst et al. [13] investigated the strain rate effect on the tensile behavior of a solid propellant with *in situ* scanning electron microscopy (SEM), and revealed interfacial debonding as the dominant fracture mechanism (mainly at the surface of the large energetic crystals). Zheng et al. [14] observed the initiation and propagation of cracks in the plerosphere/polypropylene composite with *in situ* SEM, and found a large number of micro-cracks instead of fracture cracks in particles. Wang et al. [15] characterized crack growth and propagation of a solid propellant at different stretching rates via *in situ* video imaging. Tao et al. [16] combined such techniques as acoustic emission, strain–stress curve, and high-speed photography to investigate fracture mechanism of aluminized polymer-bonded explosive (PBX) in a Brazilian test, and their *ex situ* SEM characterization demonstrated debonding at the binder-energetic crystal interface. However, the above *in situ* characterization techniques lack the penetration capability to resolve internal structure evolution in solid propellants [17].

The internal structures of PBXs/propellants have been studied using computed tomography (CT), and the microstructure effects on interfacial debonding and pore formation have been demonstrated [18–21]. Geng et al. [22] reported the compression failure of an HTPB propellant via particle fracture at low temperature, but via interface debonding and matrix tearing at room temperature. Pei et al. [23] observed the failure of an HTPB propellant under pull-and-shear loading via interface debonding. However, the limited temporal and spatial resolutions render it difficult to capture the detailed process of interfacial debonding.

Numerical simulation methods such as finite element analysis (FEM) [24] and molecular dynamics (MD) [25] are frequently employed to investigate mechanical response and internal structure of propellants under various conditions. Hou et al. [24] studied the tensile fracture mechanism of a cyclotetramethylene tetranitramine modified double-base propellants and found that the mismatch in deformation between the particles and the matrix due to the differences in their respective moduli leads to debonding at the particle–matrix interface. Zhang et al. [25] investigated the effects of neutral polymeric bonding agents (NPBAs) on interface interaction and mechanical properties of nitrate ester plasticized polyether (NEPE) propellants with MD simulations and found that NPBA can significantly improve their mechanical properties. For simplicity, many numerical models assume that the energetic crystals in a solid propellant are standard spheres. However, this approximation may fail to capture the realistic interfacial debonding evolution. Therefore, modeling based on real three-dimensional (3D) structures is necessary.

Numerical modeling utilizing CT images has been developed [26–28]. For instance, Walters et al. [29–31] developed a mesoscale modeling method based on CT data. The interfacial debonding of PBX was investigated using a cohesive traction-separation law, and it was demonstrated that the macroscopic plastic behavior is modulated by delamination of the crystal binder and plastic deformation of the binder itself. Liu et al. [32] characterized 3D internal structure and damage evolution in an NEPE propellant with *in situ* CT. CT-image-based finite element modeling was used to investigate the particle–matrix interfacial debonding in the NEPE propellant with the particle configuration taken from the actual 3D CT data. They compared two types of FEM models, one based on voxels and the other, on smooth surfaces, and demonstrated that the smooth surface FEM can effectively reduce the errors incurred by direct meshing of voxels. However, the effects of local microstructures of high energy crystal particles on interface debonding are rarely addressed.

Given the heterogeneous microstructures of energetic crystal particles and the vast variety of propellant composites, it is highly desirable to obtain the exact 3D configurations of propellant composites with such techniques as high-resolution CT. Quantitative characterizations of particle morphology, mesoscale deformation via particle tracking analysis, and the effect of morphology on deformation and fracture, are extremely underexplored with both experiments and simulations.

In the present study, the deformation and fracture process of an HTPB solid propellant subjected to uniaxial tensile loading is characterized using *in situ* synchrotron X-ray micro-CT. The influence of particle morphology on microcrack nucleation and growth is investigated via digital volume correlation (DVC) and particle track analysis (PTA) techniques. Additionally, a smooth surface-based adaptive mesh CT-image-based-FEM model is developed to study the influence of the local curvature of particle surface on microcrack nucleation and propagation. The crack preferentially nucleates at the local curvature maximum of the AP particle surface and propagates along ridge line of the upper or lower side around the AP particles. Section 2 presents the material and the methodologies for *in situ* CT tests and data analysis, followed by results and discussion in Section 3 including FEM simulation, and conclusions in Section 3.

2. Material and experiments

2.1. Material

The solid propellant composite used in this study consists of the hydroxyl-terminated polybutadiene (HTPB) matrix, ammonium perchlorate (AP) crystals, and aluminum particles, and is provided by Hubei Institute of Aerospace Chemotechnology. The scanning electron microscopy (SEM) image of the solid propellant in Fig. 1(a) shows particles with two sizes. The larger particles are AP particles (50–100 μm) and the smaller particles are aluminum particles (10–100 μm). The composite specimens are harvested from a chunk and machined into a dog-bone shape with the geometry and dimensions shown in Fig. 1b inset.

2.2. In situ CT testing

All tensile tests are conducted with a home-made uniaxial miniature material testing system (MTS; Fig. 1b) coupled with micro-CT device, implemented on X-ray fast imaging beamline (BL16U2) at Shanghai Synchrotron Radiation Facility (SSRF). The specimen is placed inside the circular PEEK window of the MTS and secured in place by two custom-made fixtures. During loading, the upper fixture is moved uniaxially along with the *z*-axis by motor, while the lower fixture remains stationary. Real-time force–displacement signal is transmitted through a piezoelectric sensor and a stepper motor in the MTS to the control computer. The beamline BL16U2 can realize single-pulse ultrafast X-ray imaging, microsecond resolved X-ray dynamic imaging and millisecond
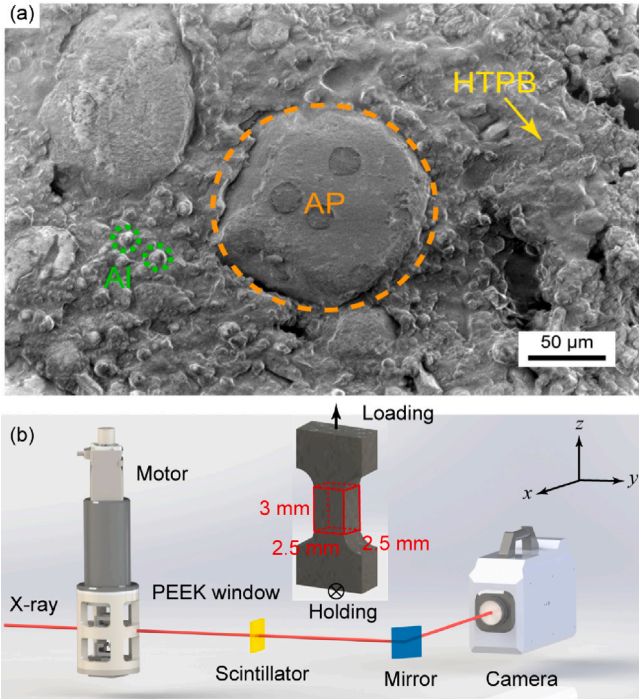
Fig. 1. (a) SEM micrograph of the as-received solid propellant. AP: ammonium perchlorate; HTPB: hydroxyl-terminated polybutadiene. (b) Experimental setup for uniaxial tensile loading with *in situ* synchrotron X-ray micro-CT. PEEK: Polyetheretherketone. Inset: Sample geometry and dimensions. The loading direction is along the *z*-axis.

resolved X-ray dynamic micro-CT for the researches on deformations and invalidations of materials under dynamic load. A cryogenic permanent magnet undulator (CPMU) cooled by liquid nitrogen as the light source provides the high-brightness X-rays. The beamline can provide pink beam mode and monochromatic beam mode [33,34]. The X-ray is white beam range from 8.7 to 30 keV. The tensile loading is applied at 0.01 s^{-1}. The real-time force–displacement signal is acquired to deduce the sample engineering stress–strain curve. At each CT sampling point, the tensile loading is paused and a CT scan is performed. The transmitted X-rays are converted into visible light by a 100 μm thickness LuAG:Ce scintillator, and the visible light is then captured by a high-speed camera (FASTCAM SA-Z, Photron, 1024 × 1024 pixels, pixel size 20 μm). The camera is equipped with a 5× magnification lens set, and the nominal pixel resolution is 3.74 μm. The field of view is 3.3 × 1.6 mm^2 (width × height). During a CT scan, the sample is rotated at a speed of 7.5° s^{-1} from 0 to 180°, and the camera continuously collected 1500 projections at a frame rate of 60 fps. For a single frame, the exposure time is set as 1 ms. Multiple scans along the height direction are performed.

2.3. Data analysis

The specific segmentation steps to identify each phase are shown in Fig. 2, starting from a representative gray-scale slice (Step 0). Firstly, Al particles are segmented via the global threshold [35] and top-hat [36] methods (Step 1, the white regions). Given the foreground markers in Step 1, the marker-controlled watershed method [37,38] is applied to refine surface profiles of the Al particles (indicated by the green dotted circles in Step 1 and Step 2). Subsequently, the threshold method is used to extract the AP particles (Step 3, the gray regions). However, the boundary effects of phase-contrast imaging and the inhomogeneity lead to abnormal local gray values for the AP particles (the black dots, Step 3). Closing operation is conducted to remove all the black spots in the AP particles, and redefine the AP particle surfaces (Step

4). However, closing operations may mistakenly result in the contact between adjacent particles (the green dotted circle in Step 4). The classical watershed algorithm is used to remove artificial particle contacts (the green dotted circle, Step 5), and individual particles are coded in different colors (Step 5). The identified AP particles are processed with the local threshold method to identify internal defects (Step 6, the red dots in particles). The microcracks are extracted by global threshold (Step 6, the red line). At last, the small island filter method is applied to remove the mis-segmentation caused by the global threshold segmentation for microcracks (e.g., the region marked by the green dotted circles). The remaining undefined regions represent the HTPB matrix (Step 7, the black regions).

Gyration tensor **G** [39–42] is used to characterize the 3D geometry of a particle, and defined in terms of the 3D voxel coordinates as

$$\mathbf{G}_{\alpha\beta}^{(m)} = \frac{1}{V^{(m)}} \sum_{\upsilon=1}^{V^{(m)}} \left(x_{\alpha_\upsilon}^{(m)} - x_{\alpha_c}^{(m)} \right) \left(x_{\beta_\upsilon}^{(m)} - x_{\beta_c}^{(m)} \right), \tag{1}$$

For particle m, $V^{(m)}$ is the total number of voxels within the particle (i.e., particle volume), and $x_{\alpha_\upsilon}^{(m)}$ or $x_{\beta_\upsilon}^{(m)}$ is the α or β coordinate of voxel υ. Here $\alpha, \beta = 1, 2, 3$ correspond to x-, y- and z-axes, respectively. Similarly, $x_{\alpha_c}^{(m)}$ or $x_{\beta_c}^{(m)}$ is the α or β coordinate of the center of mass of particle m.

The eigenvalues of gyration tensor **G**, R_1, R_2, and R_3 ($R_1 > R_2 > R_3$), are calculated to characterize the equivalent ellipsoid corresponding to a given particle [39,40]. The lengths of the three principal semi-axes of an equivalent ellipsoid follow as $\sqrt{5R_1}$, $\sqrt{5R_2}$, and $\sqrt{5R_3}$.

We introduce sphericity (S) of an equivalent ellipsoid, defined as [43]

$$S = 1 - \frac{\sum_{i>j}^{3} (R_i - R_j)^2}{2 \left(\sum_i^3 R_i \right)^2}. \tag{2}$$

S varies in the 0−1 range, and $S = 1$ for a perfect sphere. The elongation index (EI) and flatness index (FI) are introduced to characterize morphology, defined as [43,44]

$$\text{EI} = R_2/R_1, \tag{3}$$

$$\text{FI} = R_3/R_2. \tag{4}$$

Given the length of the intermediate principal semi-axis ($\sqrt{5R_2}$), a longer first principal semi-axis ($\sqrt{5R_1}$) corresponds to a lower EI, and a shorter third principal semi-axis ($\sqrt{5R_3}$) results in a lower FI.

3. Result and discussion

3.1. CT characterization of the as-received composite

The initial CT characterization of the HTPB propellant is presented in Fig. 3, including separate volume renderings of the AP particles, the Al particles, and the HTPB matrix. The AP and Al particles occupy most of the volume and are dispersed densely and uniformly in the HTPB matrix. The R_1-axis orientations are characterized in terms of polar angle θ and azimuthal angle ϕ, and are plotted in the pole figures for the AP particles and Al particles (Fig. 3). θ is measured between the z-axis and the R_1-axis, and ϕ is measured between the orthogonal projection of the R_1-axis onto the reference xy-plane and the x-axis. The pole figures demonstrated that the R_1-axis of AP particles and Al particles are randomly oriented. Similarly, R_2-axis and R_3-axis also oriented in randomly manner, indicating that the as-received solid propellant is isotropic with no preferred orientations for both the AP and Al particles.

The size of a particle is characterized with the diameter of its equivalent sphere with the same volume as the particle, i.e. the equivalent diameter. The size distributions of the AP and Al particles are presented in Fig. 4a, and their sizes are in the ranges of 25–450 μm and 13.1–100 μm, respectively. The sphericity (S) distributions of the AP and
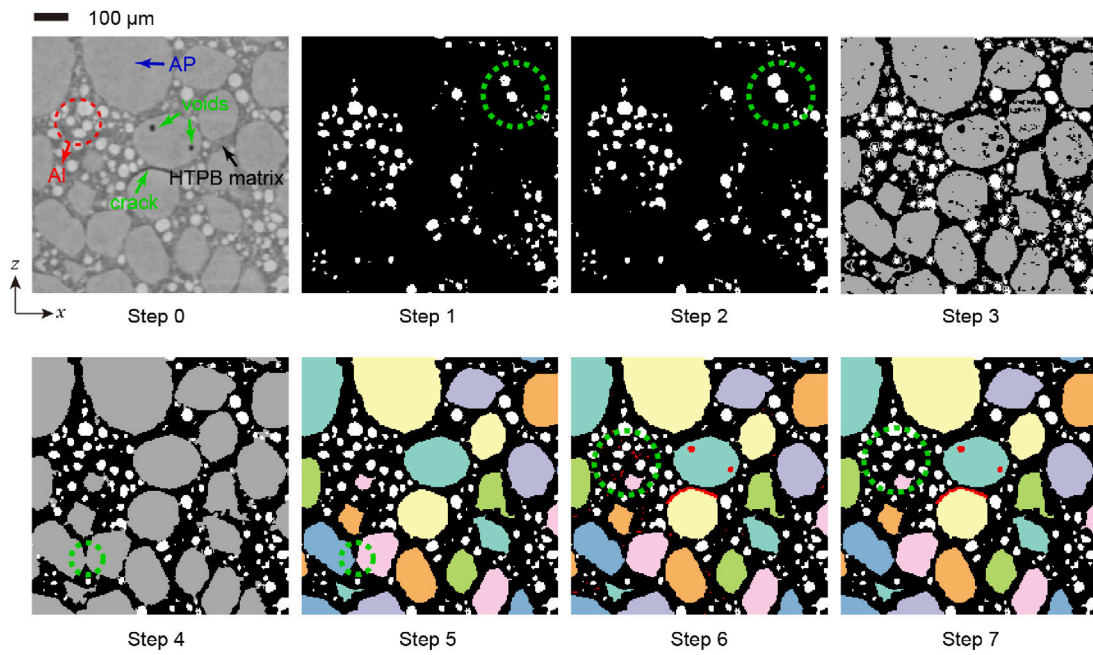
Fig. 2. Binary image segmentation procedure. Step 0: subregion of a gray-scale slice. Step 1: global thresholding and top-hat operation for Al particles. Step 2: marker-controlled watershed transform following Step 1. Step 3: thresholding operation for AP particles. Step 4: closing operation following Step 3. Step 5: classical watershed following Step 4. Step 6: global thresholding for the voids inside AP or microcracks. Step 7: island removal. The remaining undefined regions (black) are the HTPB matrix.
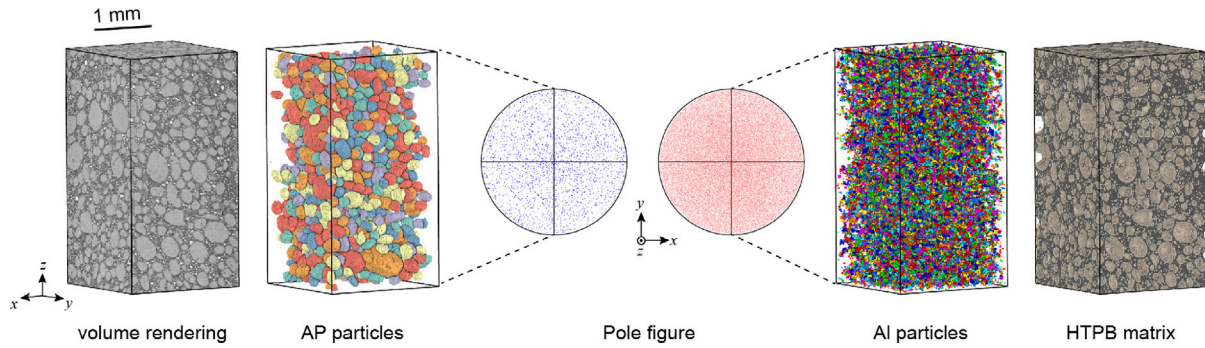

Fig. 3. CT characterization of the as-received HTPB solid propellant.
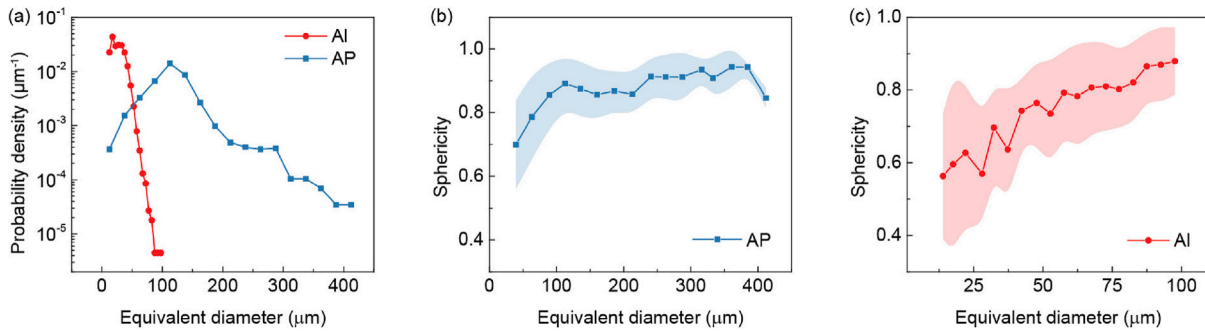

Fig. 4. Microstructural characterization of Al and AP particles. (a) Equivalent diameter distributions. (b) Sphericity as a function of equivalent diameter for AP particles. (c) Sphericity as a function of equivalent diameter for Al particles. The shaded areas in (b) and (c) denote standard deviations.

Al particles are shown in Fig. 4b and c, respectively. The sphericity of the AP particles ranges from 0.70 to 0.94. S is the lowest among the particles with an equivalent diameter of 50 μm, while the particles with an equivalent diameter of 375–425 μm are the closest to a standard sphere. For the Al particles, the standard deviation of S is large, and the lowest S is for the particles with an equivalent diameter of 30–50 μm. For both the AP particles and Al particles, S increases with increasing

equivalent diameter overall, while the standard deviation decreases. The larger particles have higher average S with smaller scatter.

3.2. Uniaxial tensile loading with in situ CT

The true/engineering stress–strain curves of the solid propellant under uniaxial tension are presented in Fig. 5, where the six CT scan
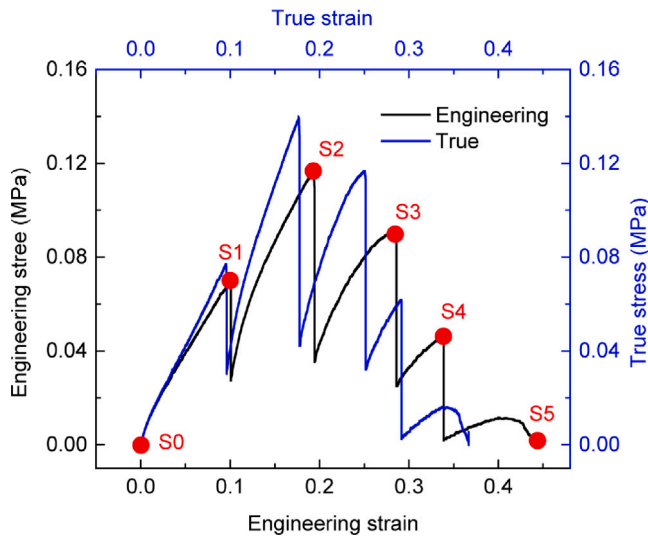
Fig. 5. Engineering stress–strain curve (black) and true stress–strain curve (blue) of the HTPB solid propellant under uniaxial tension. *In situ* CT characterization is conducted at engineering strains S0–S5.

points (S0–S5) are indicated. The engineering strain (ε) increases from 0 to 0.44 at a strain rate of $\sim 0.01\ \mathrm{s}^{-1}$, and the ultimate engineering strength is 0.12 MPa at the failure strain of 0.44. The engineering strains of 0.1, 0.19, 0.28, 0.34 and 0.44 correspond to the true strains of 0.10, 0.18, 0.25, 0.29 and 0.37, respectively. The vertical drops in engineering stress at S1–S4 are due to stress relaxation during the pause of the tensile loading for the CT scan, as commonly observed in such CT experiments [45–48]. For simplicity, the strains (ε) in this work refer to engineering strains unless stated otherwise.

The 3D volume renderings of the solid propellant are presented in Fig. 6a for the six CT scans, showing the particles, the matrix and cracks. The cracks are extracted, indexed and plotted in Fig. 6b at the six strains. Color-coding refers to the index of each crack; cracks are numbered in order from 1 to the maximum along the *z*-axis. Microcracks initially nucleate uniformly ($\varepsilon < 0.1$), and then some of them begin to coalesce, forming several microcrack concentration regions (1–3) at $\varepsilon = 0.19$. Damage regions 1–3 continue to grow at different rates ($\varepsilon = 0.28$), and the first main crack forms at $\varepsilon = 0.28$. With further damage accumulation, the macroscopic crack in region 1 continues to grow, while the damage in regions 2 and 3 change slightly ($\varepsilon = 0.34$ and 0.44). Eventually, the specimen fails completely at $\varepsilon = 0.44$. Concurrently, the two separated parts contract and rebound, resulting in the annihilation of certain microcracks in regions 2 and 3.

Inhomogeneous strain fields during the deformation of the solid propellant specimen are calculated from the CT sequence via DVC. The subset size in DVC is set as $32 \times 32 \times 32$ pixel^3, the Lagrangian strain field is obtained by calculating the correlation between the reference frame and the current frame, and then mapped on the reference frame. The reference frame is the previous frame relative to the current frame.

Fig. 6c shows the axial Lagrangian strain component (ε_{zz}) at different strains. At the beginning of microcrack nucleation ($\varepsilon \leq 0.1$, S0–S1), the specimen undergoes relatively homogeneous elongation, with several weak strain concentration regions located in the matrix between particles. During ε from 0.19 to 0.28 (S2–S3), a significant strain concentration appears in region 2. Subsequently, region 1 develops into a main crack with strain localization about 3 times the average of the specimen, and a negative strain band is detected between regions 1 and 2. After about 0.28 strain, the deformation is concentrated at the main fracture of the specimen and regions 2 and 3 shrink in response to stress relaxation due to the main crack, showing a negative strain band.

3.3. Nucleation and propagation of microcracks

To better reveal microcrack evolution, four sets of particles along with growing microcracks are selected and tracked in regions 1–3. Fig. 7a refers to region 1 (near the main crack), Fig. 7b and c refer to sub-regions A and B in region 2, respectively, and Fig. 7d refers to region 3. At this particular viewing angle, the micro cracks are visible only after 0.1 strain for the four selected particle sets. The microcracks initially appear at the top or bottom of the AP particles along the tensile direction (0.19 strain). Overall, nucleation of microcracks is largely due to tension. Subsequent crack propagation varies depending on the exact spatial arrangement of the particles. It is noteworthy that Al particles play a negligible role in the nucleation and propagation of microcracks, and are ignored at following discussion.

In Fig. 7a, microcrack propagates along the surface of an AP particle (0.28 strain), and then new microcracks form on other AP particles. Microcrack tends to cover either the upper or lower hemisphere of an AP particle, and then expand and coalesce with the neighboring microcracks (0.34 strain). Given different, random, spatial arrangements of AP particles, the propagation and coalescence of microcracks are different in Fig. 7b and c. A shear band-like strain localization observed in region 2 (Fig. 6) is largely due to the particular AP particle arrangement rather than shear, since the grain orientations change slightly. At later stages, the microcrack nucleation, propagation and coalescence cease or as a result of stress relaxation, and microcrack closure can even occur.

3.4. Particle tracking analysis

3D displacement vectors of AP particles, $\mathbf{u}(x, y, z)$, during deformation are obtained via particle tracking analysis (PTA) [49]. In terms of AP particle position, size and morphology characteristics, the tracking correlation factor C is described as

$$C = \exp\left(-\frac{1}{\sigma_g} \sqrt{\sum_\alpha \frac{\Delta x_\alpha^2}{\sigma_\alpha}} \right) \frac{\overline{V} - |\Delta V|}{\overline{V}} \frac{3 \sum_{i>j} \lambda_i \lambda_j}{\left(\sum_i \lambda_i \right)^2}. \tag{5}$$

The correlation is calculated between the current AP particle (m) and the reference AP particle (n) in two neighboring frames. Here, x_α represents the barycenter coordinates of AP particle, $\alpha = 1, 2, 3$ refer to the *x*-, *y*- and *z*-axes, respectively, and $\Delta x_\alpha = x_\alpha^{(m)} - x_\alpha^{(n)}$. σ_α and σ_g are weight factors. $\overline{V} = (V^{(m)} + V^{(n)})/2$, $\Delta V = V^{(m)} - V^{(n)}$, and V refers to AP particle volume. $\lambda_i = (R_i^{(n)}/R_i^{(m)})^{1/2}$, and R_i is calculated from gyration tensor analysis. The corresponding relationship of AP particles in two neighboring frames is obtained by iterative search for optimal correlation. The specific algorithm can be found elsewhere [49].

The displacement vectors set of AP particles at different strains are presented in Fig. 8, where each arrow illustrates the trajectory of AP particle between two neighboring frames, with the arrow representing its current position and the tail representing its previous position, and color-coding refers to displacement vector length. The field of displacement gradient along the loading direction is relatively uniform before 0.1 strain, and the displacement on the top of the field of view is relatively larger. At 0.19 strain, inhomogeneous displacements of AP particles induce strain localization as illustrated in the DVC analysis (Fig. 6c). After 0.28 strain, the AP particles at the bottom move downward (contraction due to the fracture above them), and the AP particles above the main crack undergo significant displacements, as a result of rapid fracture.

At a given strain, the AP particles are categorized into two types, with or without microcracks nucleated around AP particles. The gyration tensor analysis is performed on the AP particles with and without microcracks at 0.1 strain. The distribution of an AP particle morphology parameter p (i.e., equivalent diameter, EI and FI) can be characterized in terms of fraction (F),

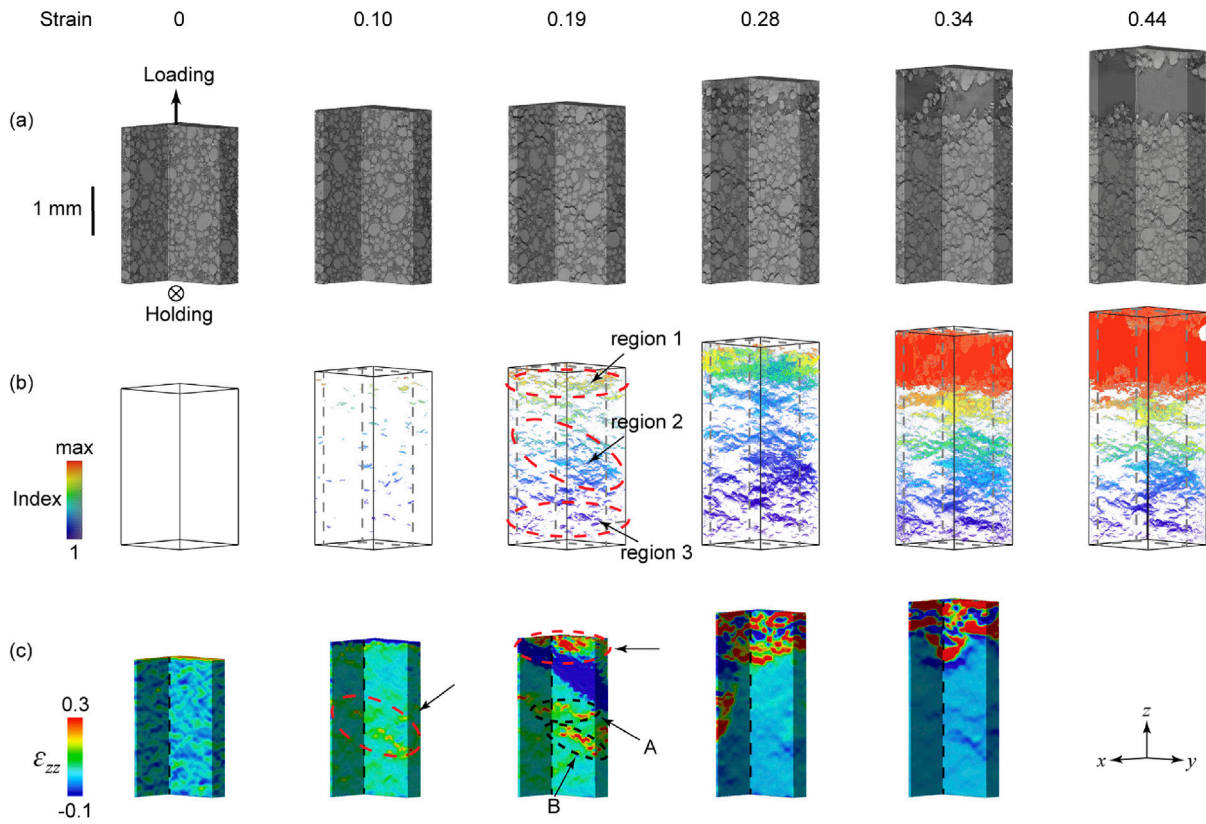$$F(q) = \frac{N(q)\big|_{p \in [\xi_q, \xi_{q+1}]}}{N}, \tag{6}$$

Fig. 6. *In situ* CT testing of the HTPB propellant. (a) 3D volume rendering of the solid propellant at different strains, (b) microcracks, with color coding referring to the index of a microcrack, and (c) axial Lagrange strain fields (ε_{zz}) obtained via DVC. The reference frame is the frame right before the current frame. Positive strain refers to tension.
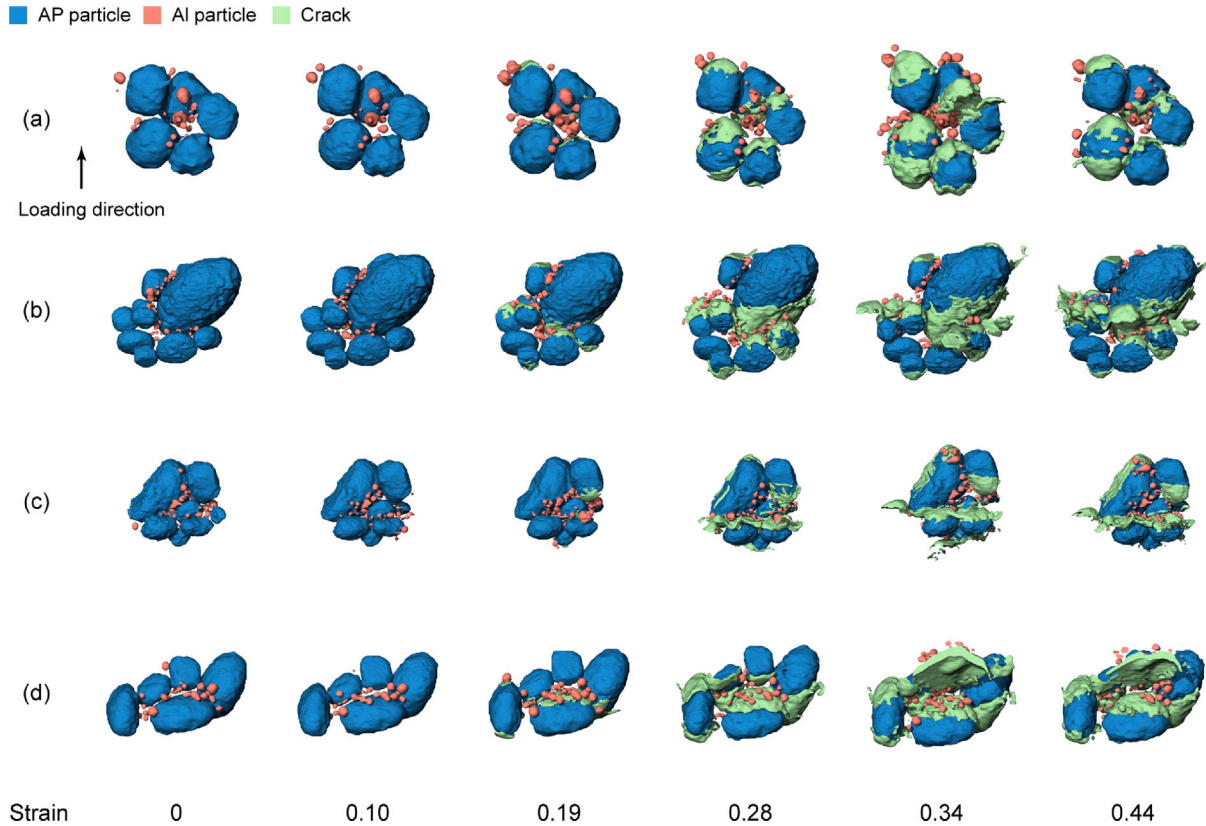

Fig. 7. Crack propagation in regions 1–3 as defined in Fig. 6b. (a) Region 1. (b) Sub-region A in region 2. (c) Sub-region B in region 2. (d) Region 3. blue: AP particle; Orange: Al particle; Green: crack. Region: crack concentration zone on the sample scale. Sub-region: a representative unit consisting of several AP particles, Al particles, matrix and microcracks within a region.
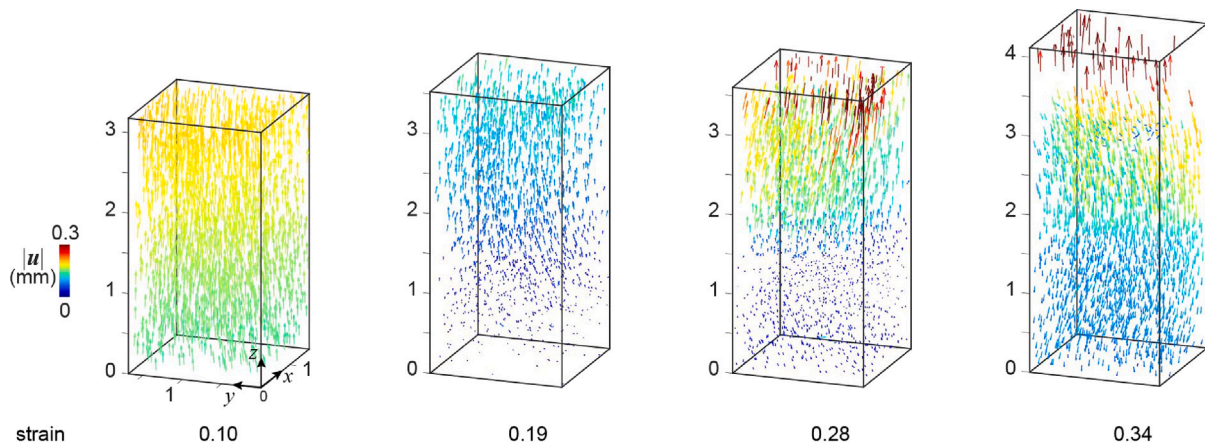
Fig. 8. 3D displacement vectors set of AP particles at different strains obtained via particle tracking analysis.
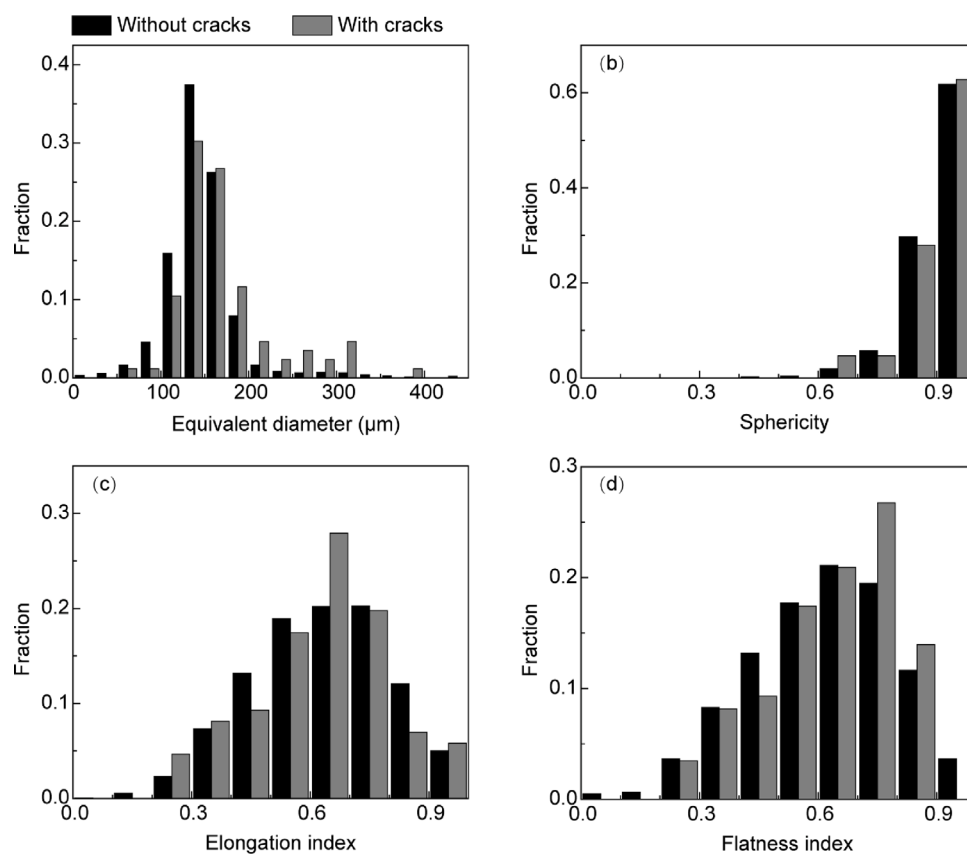

Fig. 9. Morphology statistical analysis of AP particles with and without cracks nucleated at $\varepsilon = 0.1$. (a) Equivalent diameter. (b) Sphericity. (c) Elongation index. (d) Flatness index.

where N is the total number of AP particles, and $N(q)$ is the number of AP particles whose morphology parameter p located in the qth statistical interval $[\xi_q, \xi_{q+1})$.

Fig. 9a–d present the statistical analysis of equivalent diameter, sphericity, elongation index and flatness index of the AP particles with and without microcracks nucleated around AP particles. The equivalent diameter for both types of AP particles with and without cracks are predominantly distributed between 100–200 μm, and the fraction of the AP particles with cracks with equivalent diameter over 200 μm is considerably greater than that of without cracks. The S-values of the AP particles with cracks are mainly in the range of 0.8–1, similar for the AP particles without cracks. The distributions of EI and FI are similar for the AP particles with and without cracks. For EI, the proportion of

AP particles with cracks is relatively higher in the range of 0.7–0.8. For FI, the AP particles without cracks are more evenly distributed in 0.4–0.7, and the AP particles with cracks have the highest proportion in the range of 0.7–0.8. These observations suggest that cracks prefer to nucleate around the AP particles with a larger size and a rounder shape.

Microcrack nucleation is related to AP particle morphology, either the initial AP particle morphology or the deformed AP particle morphology. To clarify this issue, the index of each AP particle is tracked back to zero strain via PTA (Fig. 10), and AP particles at zero strain and 0.1 strain are analyzed regarding their morphology parameters (EI, FI and θ). Over 80% AP particles at 0.1 strain are captured at zero strain via the PTA technique, with 100% of the AP particles with
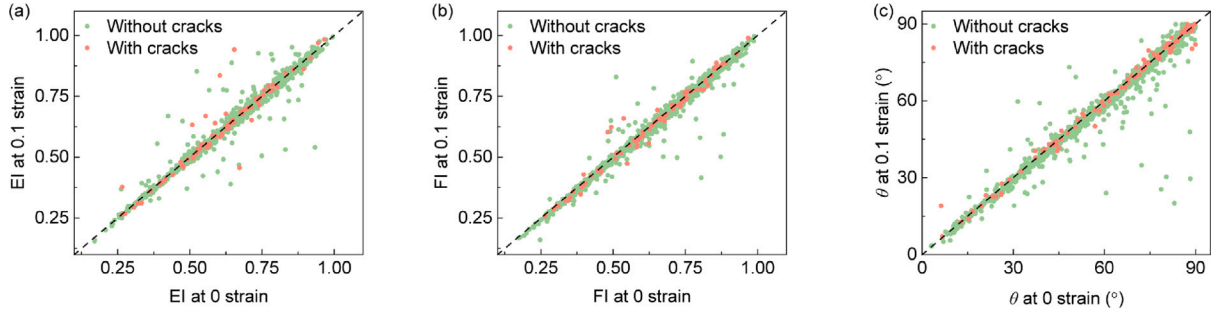
Fig. 10. Comparison of AP particle morphology at 0 strain and 0.1 strain. (a) EI. (b) FI. (c) θ (the R_1-axis orientation).

Table 1
CZM parameters for the matrix–particle interface [53].

K (MPa)	T^c (MPa)	δ^f (mm)
1500	0.5	0.02

cracks being tracked. As shown in Fig. 10, the values of EI, FI and θ at zero strain largely coincide with those at 0.1 strain, indicating that the shape and orientation of the AP particles remain almost unaltered during tensile loading, and the microcrack nucleation is dominated by the initial particle morphology.

Macroscopic interfacial debonding is related to the critical debonding stress (σ_d) [50],

$$\sigma_d = \sqrt{\frac{\gamma E K_r}{r}},\tag{7}$$

where r represents particle radius, E is Young's modulus of the matrix, γ is the interface fracture surface energy, and K_r is related to the volume fraction of particles with radius r. The above equation suggests higher σ_d for smaller particles, and this explains why debonding rarely occurs in the Al particles that are much smaller than the AP particles.

3.5. FEM modeling

To simplify calculations, most constitutive models for particle composites treat the particles as standard spheres. However, the approximation sacrifices the microstructure of particles and it is difficult to explain the micro-mechanism of particle–matrix interface debonding. Furthermore, the macroscopic failure of the sample under tensing evolved from the nanoscale microcracks. Limited by the temporal and spatial resolution of the experiment technique, it is difficult to capture the onset of microcracks debonding. Therefore, we apply the image-based finite element modeling technique to regard the as-received CT model as a finite element model to investigate microcracks nucleation.

An isolated AP particle with cracks is randomly selected and traced back to zero strain via PTA. The marching cubes algorithm [51] is applied to the AP particle surface to remove pixelization errors [32]. An adaptive mesh strategy is used to generate tetrahedral elements for the matrix and the AP particle. The cohesive zone elements (CZM) are automatically inserted on the AP particle surface. The isolated AP particle model dimensions are $750 \times 750 \times 750$ μm^3.

The Young's modulus is 5 MPa for the HTPB matrix and 32 450 MPa for the AP particle, and the Poisson's ratio is 0.495 for the matrix and 0.14 for the AP particle. The matrix is treated as a viscoelastic material, and the Prony series parameters are taken from Ref. [52]. The CZM model follows the traction separation law, and its three main parameters, the initial stiffness K, the critical stress T^c, and the critical failure displacement δ^f, are listed in Table 1.

To illustrate the influence of AP particle morphology on crack nucleation, a local elliptic paraboloid fitting method is utilized to calculate the Gaussian curvature of AP particle surface. Firstly, the outer voxels of AP particle are extracted, and a Harris operator [54] is applied to

detect the nearest 5-layer point set of a certain point v. The standard equation of an elliptic paraboloid is

$$f(x, y, z) = \frac{x^2}{a^2} + \frac{y^2}{b^2} - z = 0,\tag{8}$$

where a and b are the shape parameters of the paraboloid. Considering an elliptic paraboloid with random orientation and the origin as its vertex, the general form can be expressed as

$$\mathbf{x}^T\mathbf{R}^T\mathbf{A}\mathbf{R}\mathbf{x} + \mathbf{g}^T\mathbf{R}\mathbf{x} = 0,\tag{9}$$

where $\mathbf{x}$ is the vector from the center point v to each point in the set of neighboring points, $\mathbf{R}$ and $\mathbf{A}$ denote the rotation and shape matrices, respectively, and $\mathbf{g} = [0\ 0\ -1]^T$. The least-squares-based paraboloid fitting method is used to estimate the rotation and shape matrices [55]. The two principal curvatures at the vertex of a conic surface can be calculated by the shape parameters [56,57]. The local Gaussian curvature (K) is then estimated by multiplying the two principal curvatures and shown in Fig. 11a.

The von Mises stress (σ_{Mises}) distributions of the particle and the matrix during microcrack nucleation are obtained from the FEM simulation (Figs. 11 and 12).

Fig. 11b shows the stress distribution on the surface and inside the AP particle. At a strain of 2%, there is a stress concentration appearing on the AP particle surface, while the von Mises stress inside the AP particle only becomes noticeable above 5% strain. The stress decays along the radius from the surface of the AP particle along to the interior.

Fig. 11c and d illustrate the σ_{Mises} and stiffness degradation (SDEG) evolution on the particle–matrix interface, respectively. SDEG refers to the failure of cohesive elements under tension and ranges from 0 to 1. A higher SDEG bears a higher probability of microcrack nucleation. SDEG = 1 indicates the failure of the cohesive unit. At the particle–matrix interface, a localized stress concentration is observed at 1% strain. Significantly, the region of stress concentration coincides with the region of extreme local Gaussian curvature. At 3.5% strain, a distinct annular stress concentration zone forms at the top of the interface. Meanwhile, SDEG increases near the maximum curvature. The region of local stress concentration hardly moves and the stress increases along with tension. Since the damage at the interface is caused by tension, the microcracks nucleation area overlaps with the stress concentration. At 10% strain, an annular region appears at the interface on the bottom of the AP particle, consistent with the experimental results in Fig. 11a. Fig. 12 shows the stress distribution within the matrix. As early as 1% strain, a low magnitude stress concentration occurs in the matrix near the AP particle surface.

The above FEM simulation of debonding indicates that stress under uniaxial tension decreases in the order of the particle–matrix interface, the AP particle, and the matrix. The mismatch between the AP particle and matrix moduli is responsible for the mismatch in deformation and induces debonding at the interface. Stress concentration is closely related to the surface curvature of AP particle, and prone to occur at the maximum curvature, the preferred crack nucleation site. The microcracks then propagate along the ridge line of the upper or lower side and eventually leading to interface debonding.
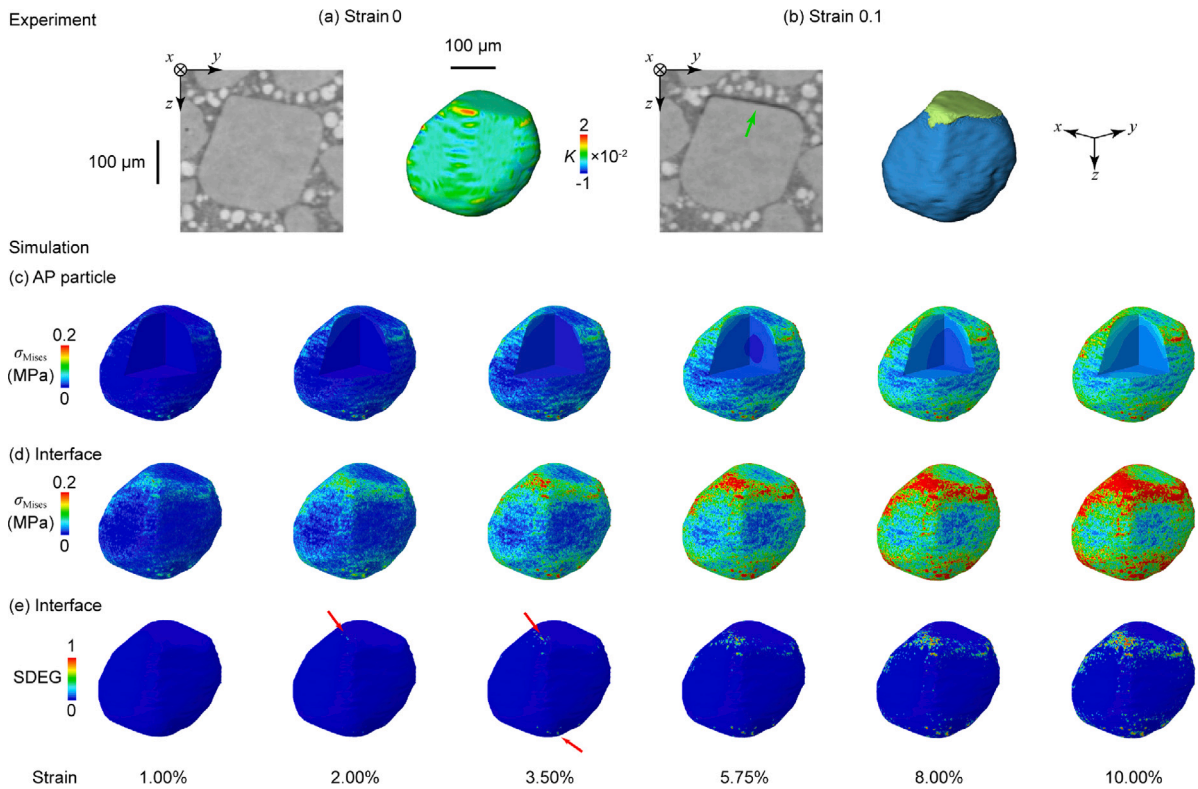
Fig. 11. (a) A *yz* slice of the specimen at strain 0 obtained from CT. The measured Gaussian curvatures (K) are mapped on the surface of the corresponding AP particle. (b) The corresponding *yz* slice at strain 0.1 and volume rendering of the AP particle (blue) and the crack (green). The green arrow refers to crack. (c) Simulated von Mises stress (σ_{Mises}) distribution on the AP particle and in it interior for different strains. (d) Simulated von Mises stress distribution at the interface for different strains. (e) Simulated stiffness degradation index (SDEG) distribution at the interface for different strains.
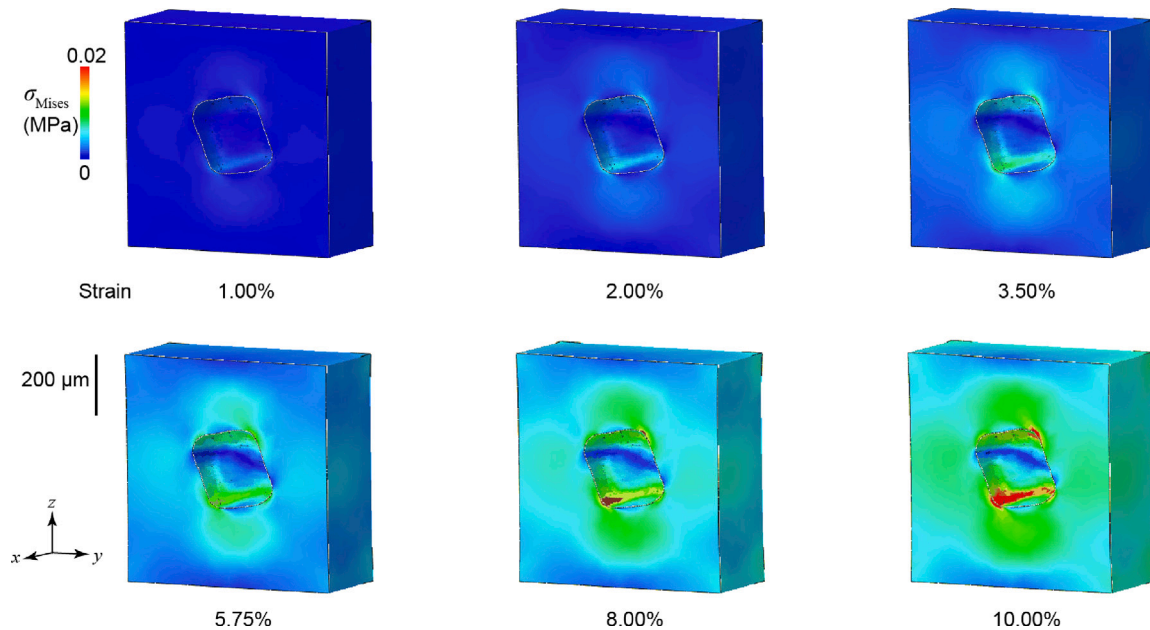

Fig. 12. Stress (σ_{Mises}) distribution in the HTPB matrix at different strains.

4. Further discussion

Mechanical damage of HTPB solid propellant composites can be achieved via matrix tearing, fracture of energetic crystal particles, and particle–matrix interface debonding. However, particle–matrix interface debonding is the dominant damage mode for HTPB solid propellants, regardless of compression or tension [22,23,50,58,59].

Interface debonding depends on particle size and surface morphology. The critical debonding stress required for spherical particles decreases with increasing particle size, i.e., larger particles are more prone to debonding. However, there normally exists surface irregularity or roughness for the crystal particles, and the particle–matrix interface can be regarded as consisting of small curved sub-surfaces with different curvatures. The sub-surfaces with larger curvature impede stress

transfer and experience greater stress [60]. Consequently, microcrack normally nucleates at the maximum curvature point on the particle surface first and then propagates along the local curvature gradient, eventually evolving into a crack covering the entire top/bottom of the particle. The cracks continue to grow along the particle surface until they cover approximately half of the AP particle. At this point, since the normal direction of the interface is almost perpendicular to the loading direction, the crack on the current particle does not undergo further growth but coalesces with the surrounding cracks, leading to a main crack and likely the failure of the specimen. The surrounding area of a main crack undergoes stress relief, giving rise to the annihilation of some of the small cracks.

5. Conclusions

An HTPB solid propellant under uniaxial tensile loading is characterized with *in situ* micro-CT, and CT-image-based-FEM modeling is applied to help reveal deformation/damage mechanisms. During uniaxial loading, the morphological and structural characteristics of AP and Al particles, and 3D strain fields and AP particle displacement fields are obtained via gyration tensor, DVC and PTA analyses. Based on tracking and statistics, an automated analysis method is proposed to analyze the relationship between microcrack nucleation and initial structure. The AP particles and Al particles remain randomly oriented in the HTPB propellant, and undergo negligible deformation during tensile loading. Microcracks are mainly nucleated via debonding induced by tension (rather than shear), preferentially at the maximum surface curvature of the AP particles, and propagate along the curvature gradient. Microcracks mainly nucleate and grow around AP particles, and Al particles play a negligible role in deformation and fracture. Larger AP particles are more prone to debond.

CRediT authorship contribution statement

G.D. Lai: Writing – original draft, Visualization, Investigation, Data curation. **L.P. Sang:** Resources. **Y.L. Bian:** Investigation. **H.L. Xie:** Resources. **J.H. Liu:** Resources, Data curation. **H.W. Chai:** Writing – review & editing, Validation, Conceptualization.

Declaration of competing interest

The authors declare that they have no known competing financial interests or personal relationships that could have appeared to influence the work reported in this paper.

Data availability

Data will be made available on request.

Acknowledgments

References

[1] L. Meda, G. Marra, L. Galfetti, S. Inchingalo, F. Severini, L. De Luca, Nano-composites for rocket solid propellants, Compos. Sci. Technol. 65 (5) (2005) 769–773.

[2] F.A. Williams, M. Barrère, N. Huang, et al., Fundamental Aspects of Solid Propellant Rockets, vol. 116, Technivision services Slough, England, 1969.

[3] K. Lysien, A. Stolarczyk, T. Jarosz, Solid propellant formulations: A review of recent progress and utilized components, Materials 14 (21) (2021) 6657.

[4] C. Rossi, S. Orieux, B. Larangot, T. Do Conto, D. Esteve, Design, fabrication and modeling of solid propellant microrocket-application to micropropulsion, Sensors Actuators A 99 (1–2) (2002) 125–133.

[5] X. Zhang, J. Zheng, H. Fang, Y. Zhang, S. Bai, G. He, High dimensional stability and low viscous response solid propellant binder based on graphene oxide nanosheets and dual cross-linked polyurethane, Compos. Sci. Technol. 161 (2018) 124–134.

[6] Y. Jiang, J. Leem, A.M. Robinson, S. Wu, A.H. Huynh, D. Ka, R.R. Zhao, Y. Xia, X. Zheng, Tailoring the mechanical and combustion performance of B/HTPB composite solid fuel with covalent interfaces, Compos. Sci. Technol. 245 (2024) 110350.

[7] K. Matouš, H. Inglis, X. Gu, D. Rypl, T. Jackson, P.H. Geubelle, Multiscale modeling of solid propellants: From particle packing to failure, Compos. Sci. Technol. 67 (7–8) (2007) 1694–1708.

[8] Y. Wu, X. Yu, X. Lin, S. Li, X. Wei, C. Zhu, L. Wu, Experimental investigation of fuel composition and mix-enhancer effects on the performance of paraffin-based hybrid rocket motors, Aerosp. Sci. Technol. 82 (2018) 620–627.

[9] J.C. Quagliano Amado, P.G. Ross, L. Mattos Silva Murakami, J.C. Narciso Dutra, Properties of hydroxyl-terminal polybutadiene (HTPB) and its use as a liner and binder for composite propellants: A review of recent advances, Propell Explos. Pyrotech. 47 (5) (2022) e202100283.

[10] H. Li, S.X. Wang, M. Li, J.S. Xu, X.G. Fan, X. Chen, Experimental research on tensile mechanical properties of NEPE propellant under confining pressure, Propell Explos. Pyrotech. 45 (11) (2020) 1769–1779.

[11] Z. Wang, H. Qiang, T. Wang, G. Wang, Tensile behaviors of thermal aged HTPB propellant at low temperatures under dynamic loading, Mech. Time-Depend. Mater. 24 (2) (2020) 141–159.

[12] H. Shekhar, Studies on stress-strain curves of aged composite solid rocket propellants, Def. Sci. J. 62 (2) (2012) 90–94.

[13] M.C. Van Ramshorst, G.L. Di Benedetto, W. Duvalois, P.A. Hooijmeijer, A.E. van der Heijden, Investigation of the failure mechanism of HTPB/AP/Al propellant by in-situ uniaxial tensile experimentation in SEM, Propellants Explos. Pyrotech. 41 (4) (2016) 700–708.

[14] Y.H. Zheng, Z.G. Shen, M.Z. Wang, S.L. Ma, Y.S. Xing, In situ observation of plerosphere/polypropylene composites in the tensile test, J. Appl. Polym. Sci. 106 (6) (2007) 3736–3742.

[15] T.Y. Wang, J.S. Xu, H. Li, W. Ding, J.M. Liu, X. Chen, Crack propagation velocity and fracture toughness of hydroxyl-terminated polybutadiene propellants: Experiments and simulations, Eng. Fract. Mech. 257 (2021) 108034.

[16] J. Tao, X.F. Wang, S.X. Zhao, The cracks formation mechanism of an aluminized polymer-bonded explosive under tensile stress, J. Energy Mater. 35 (2) (2017) 172–178.

[17] Y.Y. Zhang, S. Chen, Y. Cai, L. Lu, D. Fan, J.C. Shi, J.Y. Huang, S.-N. Luo, Novel X-Ray and optical diagnostics for studying energetic materials: A review, Engineering 6 (9) (2020) 992–1005.

[18] D. Drodge, D. Williamson, Understanding damage in polymer-bonded explosive composites, J. Mater. Sci. 51 (2016) 668–679.

[19] C.R. Siviour, P.R. Laity, W.G. Proud, J. Field, D. Porter, P. Church, P. Gould, W. Huntingdon-Thresher, High strain rate properties of a polymer-bonded sugar: their dependence on applied and internal constraints, Proc. R. Soc. A 464 (2093) (2008) 1229–1255.

[20] X. Dai, Q. Huang, F. Huang, M. Li, Y. Wen, X. Liu, The development of a confined impact test for evaluating the safety of polymer-bonded explosives during warhead penetration, Propellants Explos. Pyrotech. 40 (5) (2015) 665–673.

[21] Z. Hu, H. Luo, S. Bardenhagen, C. Siviour, R. Armstrong, H. Lu, Internal deformation measurement of polymer bonded sugar in compression by digital volume correlation of in-situ tomography, Exp. Mech. 55 (2015) 289–300.

[22] T. Geng, H. Qiang, Z. Wang, X. Wang, Z. Zhu, D. Qiao, Macroscopic and mesoscopic properties of HTPB propellant under low temperature dynamic biaxial compression loading, Polym. Test. 119 (2023) 107922.

[23] S. Pei, H. Qiang, X. Wang, S. Li, Mesoscopic failure behavior of HTPB propellant bonding interface under multi-angle pull-and-shear loading, Polym. Test. (2024) 108365.

[24] Y.F. Hou, J.S. Xu, C.S. Zhou, X. Chen, Microstructural simulations of debonding, nucleation, and crack propagation in an HMX-MDB propellant, Mater. Des. (2021) 109854.

[25] P.A. Zhang, T.Q. Li, S.M. Liu, J.R. Deng, Effects of NPBA on interface interaction and mechanical properties of NEPE propellant: Insight from molecular dynamics simulation, Comput. Mater. Sci. 171 (2020) 109135.

[26] G.D. Kosiba, R.R. Wixom, M.A. Oehlschlaeger, High-fidelity microstructural characterization and performance modeling of aluminized composite propellant, Propellants Explos. Pyrotech. 42 (12) (2017) 1387–1395.

[27] J.D. Yeager, V.W. Manner, J.A. Stull, D.J. Walters, A.M. Schmalzer, D.J. Luscher, B.M. Patterson, Importance of microstructural features in mechanical response of cast-cured HMX formulations, in: AIP Conference Proceedings, Vol. 1979, AIP Publishing, 2018.

[28] V.W. Manner, J.D. Yeager, B.M. Patterson, D.J. Walters, J.A. Stull, N.L. Cordes, D.J. Luscher, K.C. Henderson, A.M. Schmalzer, B.C. Tappan, In situ imaging during compression of plastic bonded explosives for damage modeling, Materials 10 (6) (2017) 638.

[29] D.J. Walters, D.J. Luscher, J.D. Yeager, B.M. Patterson, Investigating deformation and mesoscale void creation in HMX based composites using tomography based grain scale FEM, in: AIP Conference Proceedings, Vol. 1979, AIP Publishing, 2018.

[30] D.J. Walters, D.J. Luscher, J.D. Yeager, 3D micromechanical simulation of PBX composites, in: AIP Conference Proceedings, Vol. 2272, AIP Publishing, 2020.

[31] D.J. Walters, D.J. Luscher, J.D. Yeager, B.M. Patterson, Cohesive finite element modeling of the delamination of HTPB binder and HMX crystals under tensile loading, Int. J. Mech. Sci. 140 (2018) 151–162.

[32] Y. Liu, W. Qian, L. Wang, Y. Xue, C. Hou, S. Wu, In situ X-ray tomography study on internal damage evolution of solid propellant for carrier rockets, Mater. Sci. Eng. A 882 (2023) 145451.

[33] H. Xie, G. Du, K. Li, F. Wang, Y. Fu, Development of fast X-ray imaging beamline at SSRF, in: Eighth Symposium on Novel Photoelectronic Detection Technology and Applications, Vol. 12169, SPIE, 2022, pp. 808–813.

[34] H.-L. Xie, B. Deng, G.-H. Du, Y.-N. Fu, H. Guo, Y.-L. Xue, G.-Y. Peng, F. Tao, L. Zhang, T.-Q. Xiao, Methodology development and application of X-ray imaging beamline at SSRF, Nucl. Sci. Tech. 31 (10) (2020) 102.

[35] J.C. Russ, J.R. Matey, A.J. Mallinckrodt, S. McKay, The image processing handbook, Comput. Phys. 8 (2) (1994) 177–178.

[36] D.S. Bright, E.B. Steel, Two-dimensional top hat filter for extracting spots and spheres from digital images, J. Microsc. 146 (2) (1987) 191–200.

[37] S. Beucher, Watersheds of functions and picture segmentation, in: ICASSP'82. IEEE International Conference on Acoustics, Speech, and Signal Processing, Vol. 7, IEEE, 1982, pp. 1928–1931.

[38] R. Barnes, C. Lehman, D. Mulla, Priority-flood: An optimal depression-filling and watershed-labeling algorithm for digital elevation models, Comput. Geosci. 62 (2014) 117–127.

[39] E.T. Whittaker, A Treatise on the Analytical Dynamics of Particles and Rigid Bodies, CUP Archive, 1964.

[40] E.J. Garboczi, K. Snyder, J. Douglas, M. Thorpe, Geometrical percolation threshold of overlapping ellipsoids, Phys. Rev. E 52 (1) (1995) 819.

[41] E.J. Garboczi, Three-dimensional mathematical analysis of particle shape using X-ray tomography and spherical harmonics: Application to aggregates used in concrete, Cem. Concr. Res. 32 (10) (2002) 1621–1638.

[42] M.A. Taylor, E.J. Garboczi, S. Erdogan, D. Fowler, Some properties of irregular 3-D particles, Powder Technol. 162 (1) (2006) 1–15.

[43] H.Y. Li, H.W. Chai, X.H. Xiao, J.Y. Huang, S.N. Luo, Fractal breakage of porous carbonate sand particles: microstructures and mechanisms, Powder Technol. 363 (2020) 112–121.

[44] H.W. Chai, Z.L. Xie, X.H. Xiao, H.L. Xie, J.Y. Huang, S.N. Luo, Microstructural characterization and constitutive modeling of deformation of closed-cell foams based on in situ X-ray tomography, Int. J. Plast. 131 (2020) 102730.

[45] P. Wang, J. Wen, H. Lei, B. Xu, Y. Liu, L. Yang, D. Fang, Morphology characterization and in-situ three-dimensional strain field monitor of short carbon fiber-reinforced polymer composites under tension, Compos. Struct. 262 (2021) 113634.

[46] L. Geng, W. Wu, L. Sun, D. Fang, Damage characterizations and simulation of selective laser melting fabricated 3D re-entrant lattices based on in-situ CT testing and geometric reconstruction, Int. J. Mech. Sci. 157 (2019) 231–242.

[47] C. Löffl, H. Saage, M. Göken, In situ X-ray tomography investigation of the crack formation in an intermetallic beta-stabilized TiAl-alloy during a stepwise tensile loading, Int. J. Fatigue 124 (2019) 138–148.

[48] J. Hubálková, C. Voigt, A. Schmidt, K. Moritz, C.G. Aneziris, Comparative phenomenological study of fracture behavior of ceramic and glass foams under compressive stress using in situ X-Ray microtomography, Adv. Eng. Mater. 19 (9) (2017) 1700286.

[49] H.W. Chai, D. Fan, J.C. Yuan, L. Hu, H.L. Xie, G. Du, Q.J. Feng, W. Zhou, J.Y. Huang, Deformation dynamics of a neutron-irradiated aluminum alloy: An in situ synchrotron tomography study, Acta Mater. 243 (2023) 118493.

[50] X.G. Liu, Z.J. Wang, L. P. J., Y.H. Han, B.N. Jin, Dewetting stress of solid propellant under tensile loading, in: 2018 9th International Conference on Mechanical and Aerospace Engineering, ICMAE, IEEE, 2018, pp. 570–573.

[51] H.-C. Hege, M. Seebass, D. Stalling, M. Zöckler, A generalized marching cubes algorithm based on non-binary classifications, 1997.

[52] B. Han, Y. Ju, C. Zhou, Simulation of crack propagation in HTPB propellant using cohesive zone model, Eng. Fail. Anal. 26 (2012) 304–317.

[53] Q. Wang, G. Wang, Z. Wang, H. Qiang, X. Wang, S. Li, Z. Zhu, Biaxial tensile test and meso damage numerical simulation of HTPB propellant, Sci. Rep. 12 (1) (2022) 17635.

[54] I. Sipiran, B. Bustos, A robust 3D interest points detector based on harris operator, in: 3DOR@ Eurographics, 2010, pp. 7–14.

[55] M. Dai, T.S. Newman, C. Cao, Least-squares-based fitting of paraboloids, Pattern Recognit. 40 (2) (2007) 504–515.

[56] I. Douros, B.F. Buxton, Three-dimensional surface curvature estimation using quadric surface patches, Scanning 44 (2002).

[57] M. Yang, E. Lee, Segmentation of measured point data using a parametric quadric surface approximation, Comput. Aided Des. 31 (7) (1999) 449–457.

[58] Z.J. Wang, H.F. Qiang, G. Wang, Experimental investigation on high strain rate tensile behaviors of HTPB propellant at low temperatures, Propellants Explos. Pyrotech. 40 (6) (2015) 814–820.

[59] J.-y. Cui, H.-f. Qiang, J.-x. Wang, Experimental and simulation research on microscopic damage of HTPB propellant under tension-shear loading, AIP Adv. 12 (8) (2022).

[60] J. Williams, J. Segurado, J. LLorca, N. Chawla, Three dimensional (3D) microstructure-based modeling of interfacial decohesion in particle reinforced metal matrix composites, Mater. Sci. Eng. A 557 (2012) 113–118.